

Quantum point contact potential curvature under correlated disorder potentials

T. Aono


Department of Electrical and Electronic Systems Engineering, Faculty of Engineering, Ibaraki University, Hitachi 316-8511, Japan

M. Takahashi

Department of Physics, Tohoku University, Sendai 980-8578, Japan

M. H. Fauzi

*Center for Spintronics Research Network, Tohoku University, Sendai 980-8577, Japan
and Research Center for Physics, Indonesian Institute of Sciences, South Tangerang City, Banten 15314, Indonesia*

Y. Hirayama 

*Department of Physics, Tohoku University, Sendai 980-8578, Japan
and Center for Spintronics Research Network and Center for Science and Innovation in Spintronics,
Tohoku University, Sendai 980-8577, Japan*



(Received 5 July 2019; revised 10 May 2020; accepted 30 June 2020; published 16 July 2020)

We theoretically investigate the curvature of the confinement potential in quantum point contacts (QPCs) under a background disorder potential with Gaussian correlation functions using a noninteracting one-dimensional tight-binding model. The curvature of the potential is evaluated from the gate voltage dependence of the conductance, and the statistical average of the fitting curvature is calculated. The fitting curvature is insensitive to the original QPC confinement curvature when the characteristic length of the QPC potential is larger than the characteristic length of the disorder. In addition, the fitting curvature can be enhanced as the QPC curvature is decreased. Accidental double barrier potential formation on the top of the QPC induces enhancement of the fitting curvature. Finite-temperature effects under the disorder potential are also discussed. Similar results hold in a two-dimensional QPC tight-binding model.

DOI: [10.1103/PhysRevB.102.045305](https://doi.org/10.1103/PhysRevB.102.045305)

I. INTRODUCTION

A quantum point contact (QPC) is a narrow and short one-dimensional constriction formed on a two-dimensional electron system with split gates. The width of the constriction is controlled by the gate voltage applied to the split gates, and the length of the QPC is determined by the split gate length. The linear conductance, G , through a QPC is quantized as a function of the gate voltage in units of $2e^2/h$ [1,2], where the quantized value is the number of transverse modes in the QPC.

The microscopic QPC potential profile is revealed in the gate voltage dependence of G via the Landauer-Büttiker formula [3]. A typical QPC potential is described by the quadratic form

$$V(x) = V_0 - \frac{1}{2}m\omega_x^2x^2, \quad (1)$$

where V_0 is the potential energy at the QPC center $x = 0$, m is the electron effective mass, and $\hbar\omega_x$ is the energy to determine the curvature of the potential. The curvature has a characteristic length $l_{\text{QPC}} = \sqrt{\hbar/m\omega_x}$. The transmission probability $\mathcal{T}(\epsilon)$, through the potential (1), can be calculated analytically [4]:

$$\mathcal{T}(\epsilon) = \{1 + \exp(-2\pi(\epsilon - V_0)/\hbar\omega_x)\}^{-1}. \quad (2)$$

When \mathcal{T} is plotted as a function of the gate voltage V_0 , the range of the slope of \mathcal{T} from zero to unity is determined by $\hbar\omega_x$. In recent experiments [5–7], the Fabry-Pérot oscillation has been observed in G . In these experiments, the QPC potential is not described by Eq. (1), but has a flat-top structure so that the potential landscape acts as a quantum resonator.

The QPC potential profile is determined not only by the QPC confinement potential, but also by the background potential fluctuations due to ionized impurities in semiconductor heterostructures. The influence of the potential fluctuations has been observed in transport measurements [8,9]. The nature of the background potential fluctuations has been investigated particularly using scanning gate microscopy [10–18], which also reveals the Wigner and Kondo physics in QPC systems [19]. The potential fluctuations due to ionized impurities in semiconductor heterostructures have been addressed theoretically [20,21]; for QPC systems, these fluctuations lead the deviation from the conductance quantization [22,23]. We should emphasize that even for a very-high-mobility device, disorders still play a role in the transport properties in a confined geometry [24].

An array of 256 split gates was recently fabricated and the conductance on each gate was measured [25], which made it possible to study the statistics of the conductance of QPCs [26,27]. In Ref. [27], the gate voltage characteristics

of approximately 100 QPCs with gate lengths from 400 to 1300 nm were measured to obtain the relationship between l_{QPC} that is deduced from $\hbar\omega_x$, and the split gate length. It is reasonable to expect that l_{QPC} increases as the gate length increases. However, the experiment reveals a counterintuitive result where l_{QPC} is almost independent of the gate length. This is the most surprising observation in Ref. [27]. Moreover, the results even exhibit the opposite trend, where l_{QPC} weakly decreases as the gate length increases. This contrast indicates that the QPC potential is modified from Eq. (1). In Refs. [26,27], it was concluded that the source of the deviation comes from background disorder potential fluctuations.

Here, we investigate the conductance statistics under a disorder potential using a one-dimensional tight-binding model with an aim to understand the results for the QPC curvature in Ref. [27]. In addition to the QPC confinement potential characterized by $\hbar\omega_x$, we introduce a disorder potential with a Gaussian correlation function [28–32] to model the background potential fluctuations, instead of treating the microscopic disorder fluctuations due to the Coulomb potential of impurities. The disorder potential is characterized by the strength and the spatial correlation length. We also focus on the disorder potential effect; therefore, we examine a noninteracting QPC model.

The fitting potential curvature out of the gate voltage dependence is calculated for a given disorder potential landscape using Eq. (2). After taking the sample average of the disorder potential, the relationship between the fitting curvature and $\hbar\omega_x$ is evaluated. We show that the fitting curvature is insensitive to $\hbar\omega_x$ when l_{QPC} is larger than the characteristic length of the disorder. In addition, the fitting curvature can be enhanced as $\hbar\omega_x$ is decreased, which is consistent with the experimental results. We also show that these results are not unique to the one-dimensional QPC model, but hold for a two-dimensional QPC model as well.

The paper is organized as follows. Section II describes the tight-binding model of the QPC and the correlated disorder potential. In Sec. III, we comment on the finite-temperature smearing effect and in Sec. IV we define the yield condition, which is similar to that in Ref. [27]. Section V describes the main results of this study. The two subsequent sections discuss two simplified models to understand the results in Sec. V: Section VI is for an accidental bump model at the QPC center, and Sec. VII is for an accidental double barrier model. In Sec. VIII, we discuss the finite-temperature fitting scheme. In Sec. IX, the two-dimensional QPC tight-binding model with the correlated disorder potential is examined to compare the results with the one-dimensional tight-binding model.

II. MODEL

A. Tight-binding model

We model the QPC system with a one-dimensional tight-binding Hamiltonian,

$$H = \sum_{j,\sigma} \epsilon(j) c_{j,\sigma}^\dagger c_{j,\sigma} - t \sum_{j,\sigma} c_{j,\sigma}^\dagger c_{j+1,\sigma}. \quad (3)$$

Here, $c_{j,\sigma}^\dagger$ creates an electron with spin σ at the j th site ($-N \leq j \leq N$). The QPC potential energy is represented by the on-

site energy $\epsilon(i)$, and t is the hopping energy between nearest neighbors. The one-dimensional chain is attached to the semi-infinite leads in the local equilibrium with a Fermi distribution $f_l(\omega)$ ($l = L/R$) given by

$$f_{L/R}(\omega) = 1/\{1 + \exp(\beta(\omega - \mu_{L/R}))\} \quad (4)$$

with the Fermi energy $\mu_{L/R}$ and the temperature T with $\beta = 1/k_B T$.

We set $\epsilon(j)$ in the form [33,34]

$$\epsilon(j) = V_0 \exp\left(-\frac{(\hbar\omega_x j)^2}{4V_0 t} \frac{1}{1 - (j/N)^2}\right). \quad (5)$$

This is approximated by

$$\epsilon(j) = V_0 - \frac{(\hbar\omega_x)^2}{4t} j^2 \quad (6)$$

near the QPC center ($j = 0$), which reduces to

$$\epsilon(x) = V_0 - \frac{m\omega_x^2}{2} x^2, \quad (7)$$

where $t = \hbar^2/(2ma^2)$ and $x = aj$ with the lattice constant a . The potential shape from Eq. (5) connects the inverted parabola at the QPC center to the leads with $\epsilon(j) = 0$. In the following, $\hbar\omega_x$ is denoted by Ω_x .

B. Correlated disorder potential

Now we take into account the disorder potential due to the impurity or fluctuations in the background potential over the original QPC potential. For this purpose, a disorder potential with spatial correlations is introduced to contrast with l_{QPC} . We specifically consider the potential with the Gaussian correlations having a characteristic length ξ [30–32]:

$$V(x) = \sum_i V_{\text{md}}(i) \exp(-(x - x(i))^2/(2\xi^2))/\sqrt{\sqrt{\pi}\xi}. \quad (8)$$

The impurities are displaced at the points $x(i)$. The random potential V_{md} is an Anderson on-site disorder potential with a strength Δ :

$$\langle V_{\text{md}}(i)V_{\text{md}}(j) \rangle \equiv \Delta^2 \delta_{ij}, \quad (9)$$

where $\langle \dots \rangle$ is the disorder ensemble average. It is assumed that the impurities are located all over the sample and the summation over i is taken for all of the lattice points. Thus,

$$\begin{aligned} \langle V(x)V(x') \rangle &= \frac{\Delta^2}{\sqrt{\pi}\xi} \int dy \exp(-(x - y)^2/(2\xi^2)) \\ &\quad \times \exp(-(x' - y)^2/(2\xi^2)) \\ &= \Delta^2 \exp(-(x - x')^2/(4\xi^2)). \end{aligned} \quad (10)$$

Figure 1 illustrates the potential $V(x)$ characterized by ξ and Δ . This disorder potential $V_d(j) \equiv V(aj)$ is added to the QPC potential $\epsilon(j)$ in Eq. (5):

$$\epsilon(j) \rightarrow \epsilon(j) + V_d(j). \quad (11)$$

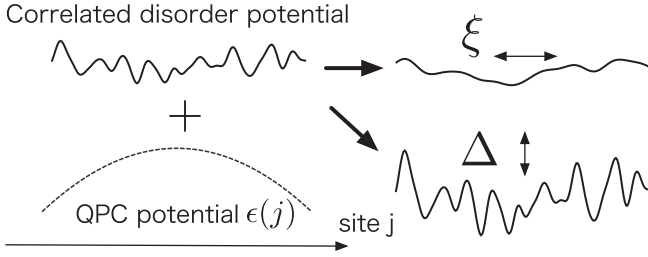


FIG. 1. The correlated disorder potential is added to the QPC potential $\epsilon(j)$. Two parameters, ξ and Δ , characterize the disorder potential: ξ controls the spatial correlation of the disorder, while Δ controls the strength of the disorder. As ξ is increased, the spatial change of the disorder becomes smoother, eventually turning into a simple potential shift in the limit of $\xi \rightarrow \infty$.

C. Landauer formula

The current I through the QPC is given by the Landauer formula:

$$I = \frac{e}{\pi\hbar} \int d\omega \mathcal{T}(\omega) (f_L(\omega) - f_R(\omega)), \quad (12)$$

with the transmission probability $\mathcal{T}(\omega)$ through a one-dimensional (1D) chain. We set $\mu_{L/R} = E_F \pm eV/2$ with the Fermi energy E_F and the bias voltage V . The linear conductance $G = \partial_V I$ is then

$$G = -\frac{e^2}{\pi\hbar} \int d\omega \mathcal{T}(\omega) \partial_\omega f(\omega), \quad (13)$$

with the equilibrium Fermi-Dirac function $f(\omega)$ with $\mu = E_F$.

D. Tight-binding parameters

In the experiment in Ref. [27], the carrier density is $n = 2.0 \times 10^{11} \text{ cm}^{-2}$, and the Fermi wavelength $\lambda_F = \sqrt{2\pi/n} = 56 \text{ nm}$. The temperature T is fixed at $T = 1.4 \text{ K}$. The split gate length is varied between 400 and 1300 nm.

The following numerical parameters were selected to reproduce this experimental setup. The lattice constant a is set to $a = \lambda_F/8$ [35], and then $a = 7.0 \text{ nm}$. We set $N = 100$, which corresponds to a 1400-nm split gate length. The hopping energy $t = \hbar^2/2m_{\text{eff}}a^2$ is 11.6 meV, where we use the effective mass $m_{\text{eff}} = 0.067m_0$ in GaAs with the electron mass m_0 in a vacuum. The Fermi energy $E_F = 0.5865784t$, which is the energy of the cosine band at $k = k_F$; $E_F = 6.8 \text{ meV}$. We set t as the unit of energy. When $T = 1.4 \text{ K}$, $k_B T/t = 0.01$. This temperature is used for all of the numerical calculations below. The QPC curvature, $\Omega_x = 2 \text{ meV}$, corresponds to $\Omega_x/t = 0.17$. The characteristic length $l_{\text{QPC}} = \sqrt{2a\sqrt{t}/\Omega_x} = 9.9 \text{ nm} \times \sqrt{t}/\Omega_x$.

III. EFFECT OF TEMPERATURE ON THE CURVATURE

Before going to the disorder QPC model, we first comment on the finite-temperature effect. For this purpose, we first discuss a clean QPC, $V_d = 0$.

In Ref. [27], the experiment is performed at $T = 1.4 \text{ K}$, while the experimental data are fitted by the Landauer formula at zero temperature. This is because the authors found that the use of either $T = 0$ or $T = 1.4 \text{ K}$ does not affect the trends

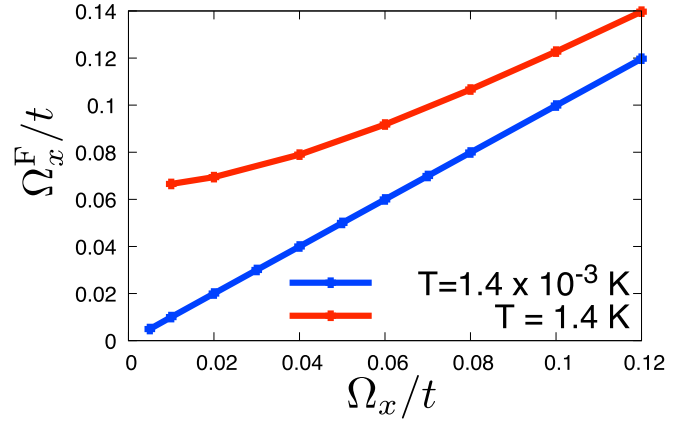


FIG. 2. Fitting curvature Ω_x^F/t as a function of the QPC curvature Ω_x/t , for $T = 1.4 \times 10^{-3} \text{ K}$ (blue) and $T = 1.4 \text{ K}$ (red).

[36]. The conductance G in Eq. (13) at zero temperature with Eq. (2) is then

$$G(V_0) = \frac{e^2}{h} \frac{2}{(1 + \exp(2\pi(V_0 - E_0^F)/\Omega_x^F))}. \quad (14)$$

Here E_0^F and Ω_x^F are the fitting parameters from Eq. (2) (the superscript ‘‘F’’ denotes a fitting parameter). Next, we introduce an extra fitting parameter, G_0^F , instead of the factor of 2 (spin degeneracy) in Eq. (14), and then use the fitting function

$$G(V_0) = \frac{e^2}{h} \frac{G_0^F}{(1 + \exp(2\pi(V_0 - E_0^F)/\Omega_x^F))}, \quad (15)$$

with the fitting parameters G_0^F , E_0^F , and Ω_x^F . The necessity of G_0^F is explained below in Sec. IV. To perform the fitting, the `scipy.optimize.curve_fit` [37] PYTHON routine was used for the nonlinear least-squares optimization method. When $T = 0$, $\Omega_x^F = \Omega_x$ for the parabolic potential [4], as it should be.

For a given Ω_x , G is calculated as a function of V_0 , and the fitting is applied to obtain Ω_x^F . Figure 2 shows Ω_x^F plotted as a function of Ω_x for $T = 1.4 \times 10^{-3} \text{ K}$ and 1.4 K . At $T = 1.4 \times 10^{-3} \text{ K}$ (blue curve), $\Omega_x^F = \Omega_x$ as expected. At $T = 1.4 \text{ K}$ (red curve), Ω_x^F increases with Ω_x ; Ω_x^F qualitatively captures the trend of Ω_x in G .

However, a quantitative deviation is observed: $\Omega_x^F > \Omega_x$. This is explained as follows. When $T = 1.4 \text{ K}$, $k_B T/t = 0.01$. Thus, $k_B T$ is comparable to Ω_x in Fig. 2. At a finite temperature, G is determined by these two energy scales; $\mathcal{T}(\omega)$ changes over the range of Ω_x , while the differentiation of the Fermi-Dirac function changes over the range of $k_B T$. The thermal energy then smears the change in $\mathcal{T}(\omega)$, and if G is fitted by Eq. (15), $\Omega_x^F > \Omega_x$. The thermal smearing is dominant when Ω_x is decreased, i.e., a longer QPC.

In Ref. [27], zero-temperature fitting was performed because the finite-temperature fitting gives a similar trend. This indicates that the QPC is not simply described by a simple quadratic potential model. Therefore, we now introduce disorder potentials. We discuss the finite-temperature fitting later in Sec. VIII to clarify the role of the disorder potentials.

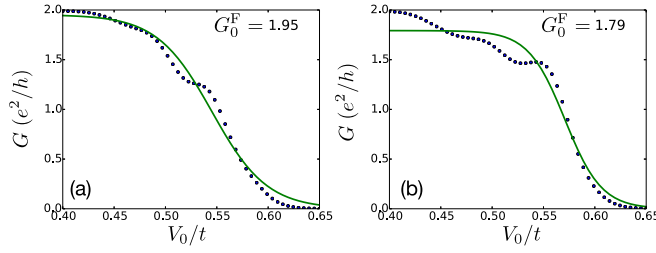


FIG. 3. Sample fitting: the yield condition is satisfied for (a) and not for (b). The blue points show G numerically calculated with a sample V_d at $T = 1.4$ K. The green lines are the fitting curves. The value of G_0^F is indicated in each subgraph.

IV. YIELD CONDITION AND SAMPLE AVERAGE

Now we introduce the disorder potential, V_d . Under the disorder potential, the conductance quantization is not perfect. In the experiments in Refs. [25,27], a yield criterion for the device is introduced: whether the first two or three conductance plateaus occur within $\pm 0.1G_0$ or not. If this yield criterion is not satisfied, then the conductance data are rejected from the statistical average. Since this “quantum yield” is a core idea in the experiments, we incorporate this concept into our numerical calculations. Under the yield criterion, the fitting procedure is not simply applying Eq. (14) to deduce E_0^F and Ω_x^F . The fitting function actually requires an extra parameter to judge the criterion. This is the reason why we have introduced an extra parameter G_0^F in Eq. (15).

With G_0^F , we now introduce a similar yield criterion, as follows. For a given disorder potential $V_d(j)$, G is calculated as a function of V_0 at $T = 1.4$ K. The fitting function for the conductance, Eq. (15), is then applied to deduce G_0^F , E_0^F , and Ω_x^F . If G_0^F satisfies the following condition,

$$1.9 < G_0^F < 2.1, \quad (16)$$

then the disorder sample is accepted; otherwise it is rejected. Note that G_0^F can exceed 2, despite the numerical data of G within $2e^2/h$, as a single channel QPC model. This is because the fitting formula (15) is applied without further restrictions such as $G_0^F \leq 2.0$. Such disorder samples are kept as long as condition (16) is satisfied. The statistical average is taken over the accepted samples to obtain the average curvature $\langle \Omega_x^F \rangle$ and its variance. Examples of the fitting are shown in Fig. 3, where blue points indicate the numerical data for a given disorder potential and green lines indicate the fitting curves. Here, the case in Fig. 3(a) satisfies the yield condition and the case in Fig. 3(b) is rejected. Note that we discuss whether the validity of the numerical results is maintained when condition (16) is changed in Sec. V B.

V. CURVATURE UNDER DISORDER POTENTIALS

Next we discuss the curvature of QPCs under the disorder potentials with various values of ξ and Δ . In the experiment in Ref. [27], the statistics of Ω_x^F are measured with different QPC split gate lengths. Here we change Ω_x , which equivalently changes the QPC length, as shown in Fig. 4(a). One hundred

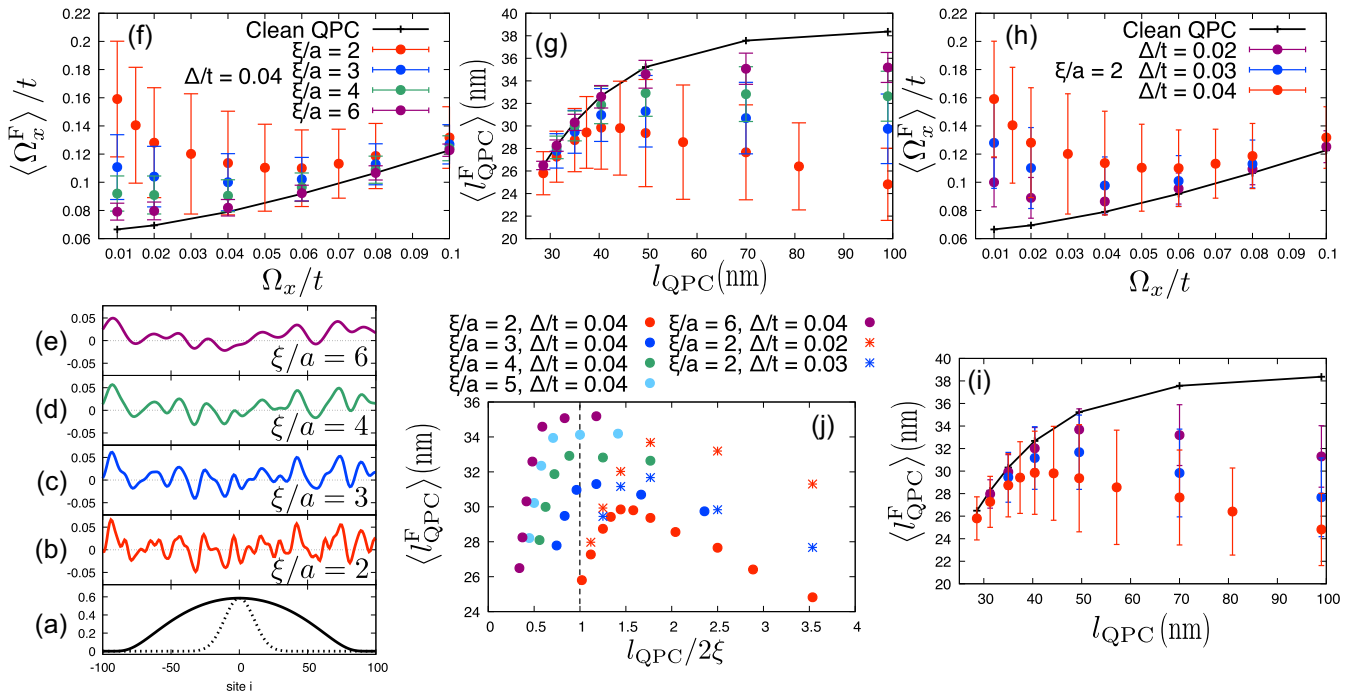


FIG. 4. QPC curvature under disorder potentials. (a) QPC potential profile: clean QPC potential with $\Omega_x/t = 0.02$ (black solid line) and $\Omega_x/t = 0.1$ (black dotted line). (b–e) Correlated disorder potentials with (b) $\xi/a = 2$, (c) $\xi/a = 3$, (d) $\xi/a = 4$, and (e) $\xi/a = 6$. $\Delta/t = 0.04$. (f) $\langle \Omega_x^F \rangle$ versus Ω_x for various values of ξ with $\Delta/t = 0.04$. The error bars represent the variance of $\langle \Omega_x^F \rangle$. (g) $\langle l_{\text{QPC}}^F \rangle$ versus l_{QPC} for the same values of ξ and Δ in (f). (h) $\langle \Omega_x^F \rangle$ versus Ω_x for various values of Δ with $\xi/a = 2.0$. (i) $\langle l_{\text{QPC}}^F \rangle$ versus l_{QPC} for the parameters in (h). In (f–i), the solid lines represent the results for the clean QPC. (j) The horizontal axis is normalized by $l_{\text{QPC}}/2\xi$ in (g) and (i). The case for $\xi/a = 5$ and $\Delta/t = 0.04$ is added. Error bars are not shown.

disorder samples are then prepared for a given parameter set of Ω_x , ξ , and Δ to calculate G as a function of V_0 . Figures 4(b)–4(d) show samples of $V_d(j)$ with four different values of ξ and $\Delta/t = 0.04$.

A. Numerical results

In Fig. 4(f), $\langle \Omega_x^F \rangle$ is plotted as a function of Ω_x with various values of ξ . The error bar for each point indicates the variance of $\langle \Omega_x^F \rangle$. The result for the clean QPC is also plotted as a reference. When $\xi/a = 6$, $\langle \Omega_x^F \rangle$ is almost identical to that for the clean QPC. In this case, the disorder potential turns into a potential energy shift and there is little influence on $\langle \Omega_x^F \rangle$. When ξ is shorter, the deviation from the clean QPC result becomes clearer. For example, when $\xi/a = 3$, $\langle \Omega_x^F \rangle$ is clearly larger than the clean QPC result for $\Omega_x/t < 0.05$, while $\langle \Omega_x^F \rangle$ is still similar to that of the clean QPC for $\Omega_x/t > 0.05$. When $\xi/a = 2$, the deviation is observed up to $\Omega_x/t \sim 0.08$. Moreover, $\langle \Omega_x^F \rangle$ is clearly enhanced as Ω_x is decreased. This result is in contrast with the clean QPC case.

Figure 4(g) shows $\langle l_{\text{QPC}}^F \rangle = \sqrt{\hbar^2/m\langle \Omega_x^F \rangle}$ as a function of l_{QPC} . The deviation of $\langle l_{\text{QPC}}^F \rangle$ is evaluated using $\sqrt{1/(x + \Delta x)} \simeq \sqrt{1/x} - \frac{1}{2}(1/x)^{3/2}\Delta x$. The fitting length $\langle l_{\text{QPC}}^F \rangle$ changes slowly as a function of l_{QPC} . This is also observed for the clean QPC because of the temperature smearing effect, as discussed in Sec. III. The disorder potential induces a new feature. When ξ is decreased, $\langle l_{\text{QPC}}^F \rangle$ is suppressed as l_{QPC} is increased. This is in contrast to the clean QPC case. In Fig. 4(b) of Ref. [27], the effective QPC length is approximately 22 nm, and it is almost independent when compared to the change in the gate length. In some cases, the effective length decreases as the QPC length is increased. The results of Fig. 4(g) when ξ is small are consistent with these experimental results, except that the length is larger than the experiment.

Figure 4(h) shows $\langle \Omega_x^F \rangle$ as a function of Ω_x for various values of Δ with $\xi/a = 2.0$, and Fig. 4(i) shows $\langle l_{\text{QPC}}^F \rangle$ as a function of l_{QPC} . These figures show that a weaker disorder potential is similar to the clean QPC potential, as expected.

Finally, we comment on the comparison between l_{QPC} and ξ . Equation (10) shows the disorder correlation length is 2ξ , which competes with l_{QPC} . Figure 4(j) shows $\langle l_{\text{QPC}}^F \rangle$ as a function of $l_{\text{QPC}}/2\xi$. The extra result with $\xi/a = 5.0$ and $\Delta/t = 0.04$ is added. When $l_{\text{QPC}}/2\xi \lesssim 1$, $\langle l_{\text{QPC}}^F \rangle$ behaves like the clean QPC. In this regime, the disorder potential simply shifts the QPC potential energy. When $l_{\text{QPC}}/2\xi \gtrsim 1$, the deviation from the clean QPC becomes clearer. In this regime, the disorder potential creates a subpotential landscape on top of the QPC potential, and, as a result, the disorder potential can effectively influence G .

B. Robustness of the results

The numerical results obtained so far have been obtained assuming two conditions: the yield condition, Eq. (16), and the range of gate voltage used for the fitting. Here, we discuss whether the validity of the results is maintained when these conditions are changed.

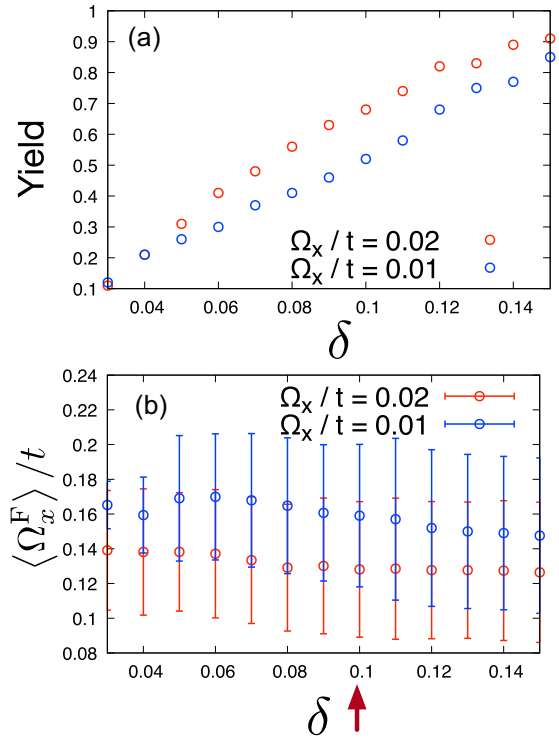


FIG. 5. Yield condition dependence: (a) yield range δ versus the yield when $\Omega_x/t = 0.02$ (red) and 0.01 (blue) with $\xi/a = 2$ and $\Delta/t = 0.04$. (b) $\langle \Omega_x^F \rangle$ versus δ .

First, we discuss the robustness against the yield condition. Instead of the yield condition, Eq. (16),

$$(2 - \delta) < G_0^F < (2 + \delta) \quad (17)$$

can be chosen, with a certain number δ , as the yield condition. Figure 5 shows the δ dependence of the yield, i.e., the ratio between the number of accepted samples over 100 samples, and $\langle \Omega_x^F \rangle$ for $\Omega_x/t = 0.01$ and 0.02 and $\xi/a = 2$. The yield is dependent on δ , as shown in Fig. 5(a). However, $\langle \Omega_x^F \rangle$ is weakly dependent on δ , and remains within the error bars. Thus, we consider that the case of $\delta = 0.1$ represents a typical example of numerical calculations.

Next, we examine the robustness against the range of gate voltage. Only the first channel in the QPC transport is taken into account; when G reaches the $2e^2/h$ plateau, G remains constant even if the gate voltage is changed. When the fitting is applied for a longer plateau, the yield condition is likely to be satisfied, and the yield is then increased. This means that the fitting values may be dependent on the gate voltage cutoff. In experiments, the gate voltage cutoff is not arbitrary, but is determined by the second channel of the QPC.

In the experiment in Ref. [27], the range of plateau ΔE_{12} varies from approximately 2 to 3 meV, depending on the QPC length. To compare with this result, the range of the gate voltage is examined: $V_{\text{min}}/t < V_0/t < 0.65$ with several values of V_{min} . So far, $V_{\text{min}}/t = 0.4$ is selected, which corresponds to $V_{\text{min}} = E_F - \delta E_{12}$ with $\delta E_{12} = 2.17$ meV. Two other cases are examined: $V_{\text{min}}/t = 0.45$, which is equal to $\delta E_{12} = 1.5$ meV, and $V_{\text{min}}/t = 0.37$ with $\delta E_{12} = 2.5$ meV. The yield condition, Eq. (16), is used. Figure 6(a) shows the yield as a function of

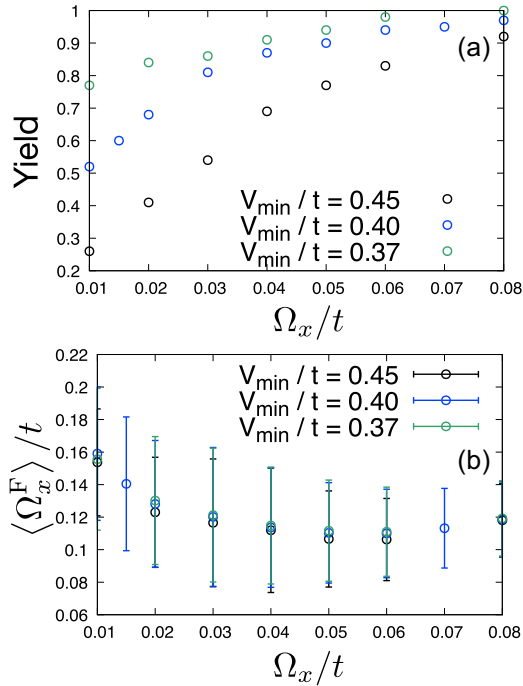


FIG. 6. Yield and curvature under the voltage range $V_{\min}/t < V_0/t < 0.65$ with $V_{\min}/t = 0.45, 0.40$, and 0.37 . The disorder potential parameter is $(\xi/a, \Delta/t) = (2, 0.04)$. (a) Yield as a function of Ω_x and (b) $\langle \Omega_x^F \rangle$ as a function of Ω_x .

Ω_x . For a smaller value of Ω_x , the yield deviates from unity. The yield values are dependent on V_{\min} . However, as shown in Fig. 6(b), $\langle \Omega_x^F \rangle$ is not dependent on V_{\min} . Therefore, the results with $\langle \Omega_x^F \rangle$ are robust against the choice of V_{\min} within the experimental setup.

VI. ACCIDENTAL BUMP MODEL

In this section, we discuss a possible mechanism for the enhancement of $\langle \Omega_x^F \rangle$ by the disorder potential. The disorder potential can accidentally create bumps near the QPC center. If the curvature of a bump potential is larger than Ω_x , then the fitting curvature Ω_x^F can be larger than Ω_x . We examine this enhancement mechanism of $\langle \Omega_x^F \rangle$.

For this purpose, we consider a simple situation: one bump at the QPC center with a curvature Ω_d . In addition to the QPC potential $\epsilon(j)$, the extra potential $\epsilon_d(j)$ is added in the form of Eq. (5): $\epsilon_d(j) = \epsilon_0(j; \Omega_x = \Omega_d, V_0 = d)$ with the bump height d . Figures 7(a) and 7(b) show the potential landscapes for $\Omega_x > \Omega_d$ and $\Omega_x < \Omega_d$, respectively. Figure 7(c) shows Ω_x^F as a function of Ω_d . As Ω_d is increased, Ω_x^F is enhanced by the bump. Note that when Ω_d is further increased, Ω_x^F decreases because keeping the potential height constant and increasing Ω_d result in a narrow (sharp) barrier. When the barrier is very narrow, tunneling is enhanced and the effect of the bump gradually fades out.

Now we discuss the connection between Ω_d and the correlated disorder potential, where the correlation function is given by

$$\langle V(x)V(0) \rangle = \Delta^2 \exp\left(-\frac{x^2}{4\xi^2}\right), \quad (18)$$

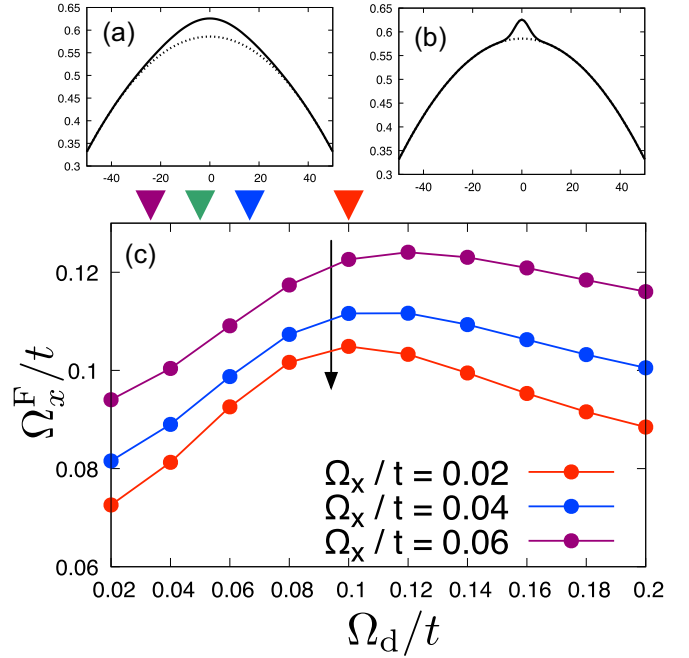


FIG. 7. Accidental bump model: (a, b) The dotted lines represent $\epsilon(j)$ with $\Omega_x/t = 0.02$. The solid lines represent $\epsilon(j) + \epsilon_d(j)$ with $d/t = 0.04$, and (a) $\Omega_d/t = 0.02$ or (b) $\Omega_d/t = 0.1$. (c) Fitting curvature Ω_x^F as a function of Ω_d for $\Omega_x/t = 0.02, 0.04$, and 0.06 . Color triangles on the top of the figure indicate the values of Ω_d for $\xi/a = 2$ (red), 3 (blue), 4 (green) and 6 (purple) with $\Delta/t = 0.04$ in Fig. 4(f).

with $\langle V(0)^2 \rangle = \Delta^2$. When $x \sim 0$, the right-hand side of Eq. (18) is expanded as

$$\langle V(x)V(0) \rangle \sim \Delta^2 \left(1 - \frac{x^2}{4\xi^2}\right). \quad (19)$$

Then $V(x)$ can be approximated near $x = 0$ by the parabolic form:

$$V(x) - V(0) = \pm \Delta \frac{x^2}{4\xi^2}. \quad (20)$$

Let us consider the inverted parabolic potential with $V(x) - V(0) = -\Delta \frac{x^2}{4\xi^2}$. The effective curvature ω_d of the bump potential is defined by $V(x) = V(0) - m(\omega_d x)^2/2$, and we let $\Omega_d = \hbar\omega_d$, which results in

$$\Omega_d = t \sqrt{\frac{\Delta}{t}} \left(\frac{\xi}{a}\right)^{-1}, \quad (21)$$

where we have used $t = \hbar^2/(2ma^2)$. The inverted parabolic potential is smoothly terminated, as in Eq. (5). In Fig. 7(c), the color triangles indicate Ω_d for the various values of ξ in Fig. 4(f). The enhancement of $\langle \Omega_x^F \rangle$ as ξ decreases in Fig. 4(f) is correlated with the enhancement of Ω_x^F by the increase of Ω_d . The accidental bump model can thus partly explain the enhancement of $\langle \Omega_x^F \rangle$. However, Ω_x^F decreases with Ω_x as indicated by the black arrow in Fig. 7(c). This trend is opposite that in Fig. 4(f). Thus, the accidental bump model fails to explain an important feature of the disorder potential model.

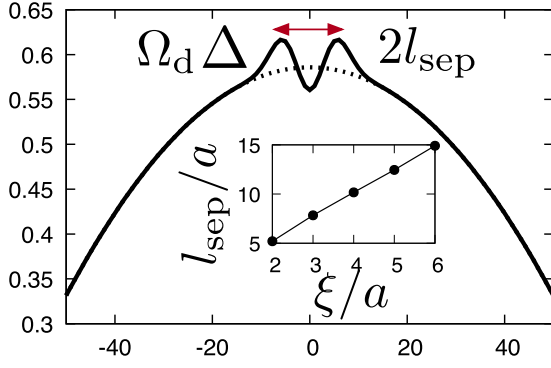


FIG. 8. Double barrier potential: the dotted line represents $\epsilon(j)$, and the solid line represents $\epsilon(j) + V_{DB}(j)$. Inset: Sample average of l_{sep} as a function of ξ for the correlated disorder potential (8).

VII. ACCIDENTAL DOUBLE BARRIER MODEL

The single-bump model is thus insufficient; therefore, we next examine a slightly more complicated bump structure, a double barrier potential model with double-bump barriers in addition to a dip structure at the QPC center. Here, the potential V_{DB} is given by

$$V_{DB}(x) = \begin{cases} +\Delta - m\omega_d^2(x - l_{sep})^2/2 & (x \sim l_{sep}) \\ -\Delta + m\omega_d^2x^2/2 & (x \sim 0) \\ +\Delta - m\omega_d^2(x + l_{sep})^2/2 & (x \sim -l_{sep}). \end{cases} \quad (22)$$

The potential is characterized by three parameters: the curvature Ω_d , the potential depth Δ , and a half of the peak-to-peak distance l_{sep} of the bumps. The first two parameters are the same as those in the accidental bump model. Each parabolic term in Eq. (22) is smoothly terminated, as in Eq. (5) [38]. The potential profile is shown in Fig. 8. The potential induces a quantum-dot-like confinement potential at the QPC center, and a quasibound state on the top of the QPC will likely appear. For the disorder potential, Eq. (8), l_{sep} is numerically evaluated. For this purpose, the disorder potential is generated over 10 000 sites for a given value of ξ , and the peak-to-peak separation of the potential is evaluated within the sites. The half of the average, l_{sep} , is plotted as a function of ξ in the inset of Fig. 8, where l_{sep} is proportional to ξ .

Numerical calculations with the double barrier potential are performed to understand the results with the disorder potential. For this purpose, the calculation is performed with the parameter set (l_{sep}, Ω_d) of the double barrier potential equivalent to the disorder potential with ξ . The correspondence between the parameters of both models is summarized

TABLE I. Relationship between ξ of the disorder potential and parameter set (l_{sep}, Ω_d) of the accidental double barrier potential.

Disorder potential	Accidental double barrier potential	
ξ/a	l_{sep}/a	Ω_d/t
2	5.20	0.10
3	7.84	0.067
4	10.2	0.050
6	14.9	0.033

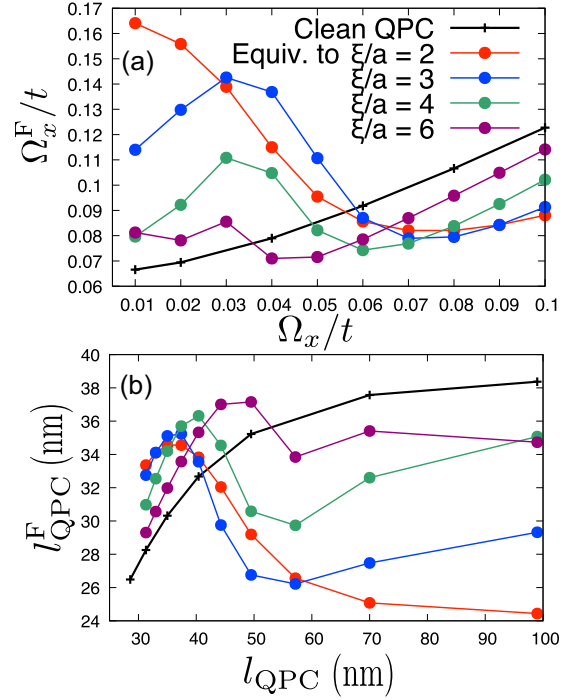


FIG. 9. Accidental double barrier model: (a) Ω_x^F versus Ω_x . The value of ξ shown in the legend indicates that the calculation is performed using the parameter set (l_{sep}, Ω_d) , which is equivalent to the value of ξ for the disorder model in Table I. $\Delta/t = 0.04$. (b) l_{QPC}^F versus l_{QPC} for the same values of ξ and Δ in (a).

in Table I. Figure 9(a) shows Ω_x^F versus Ω_x of the double barrier model. An enhancement of Ω_x^F appears when Ω_x decreases. The enhancement is clearer for the parameter set with smaller values of ξ . These results are consistent with those in Fig. 4(f). Figure 9(b) shows l_{QPC}^F versus l_{QPC} , which also shows the suppression of l_{QPC}^F as l_{QPC} increases, as in Fig. 4(g). In this way, the accidental double barrier model can explain the results for the correlated disorder model.

The origin of the enhancement is evident in the $G-V_0$ characteristics. Figure 10(a) shows the matrix of plots of $G-V_0$ with Ω_x and the parameter set (l_{sep}, Ω_d) equivalent to the value of ξ for the disorder model in Table I; the value of Ω_x^F is indicated in each subpanel. The enhancement of Ω_x^F in Fig. 9(a) comes from the shoulder or hump structures in G . Larger values of Ω_x^F come from the substructures. Figure 10(b) shows several examples of $G-V_0$ curves for the correlated disorder model with large values of Ω_x^F for $\xi/a = 2$ and $\Omega_x/t = 0.02$. The

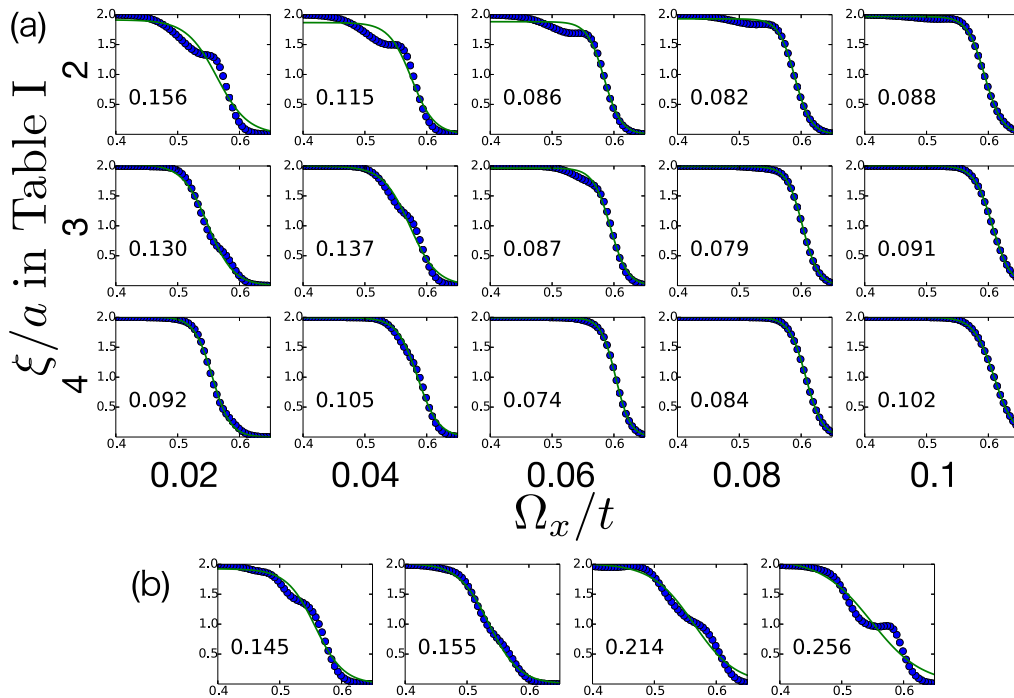


FIG. 10. (a) Matrix of plots of G versus V_0/t for the accidental double barrier model with the parameter set $(l_{\text{sep}}, \Omega_d)$ equivalent to the value of ξ for the disorder model in Table I. The values of ξ and Ω_x for each subpanel are indicated at the outer edge of the matrix. (b) Examples of G versus V_0/t for the correlated disorder model: $\Omega_x/t = 0.02$, $\xi/a = 2.0$, and $\Delta/t = 0.04$. In (a) and (b), G is plotted in units of e^2/h , the blue points show the numerical result and the green lines are the fitting curves, and the value of Ω_x^F is designated in each subpanel.

substructures in the G - V_0 curves are similar to those in the accidental double barrier model.

In summary, when the original QPC potential is flat, disorder causes double or multiple peak potentials, which result in resonant-type hump structures in G . Such structures increase Ω_x^F calculated by fitting.

VIII. FINITE-TEMPERATURE FITTING

We now consider the finite-temperature effect. So far we have used the zero-temperature fitting scheme for finite-temperature conductance. This is because the experiment claims that both zero-temperature fitting and finite-temperature fitting have similar trends. In this section, we examine this point.

The numerical data are now fitted by the finite-temperature Landauer formula, Eq. (13), at $T = 1.4$ K, with the fitting parameters G_0^F , E_0^F , and Ω_x^F , as in Eq. (15) [39]. Figure 11 shows a comparison between the zero-temperature fitting and finite-temperature fitting for the cases of $\xi/a = 2$ and $\xi/a = 6$, as well as for the clean QPC model. The notation of “0/T” refers to the zero- or finite-temperature fitting; the notations for the average curvature $\langle \Omega_x^{F(0/T)} \rangle$ and that for the fitting QPC length $\langle l_{\text{QPC}}^{F(0/T)} \rangle = \sqrt{\hbar^2 / (m \langle \Omega_x^{F(0/T)} \rangle)}$ are also used below [40].

For the clean QPC model, $\Omega_x^{F(T)} = \Omega_x$, as shown by the grey line in Fig. 11(a), which is an expected result. For the disorder QPC model, when $\xi/a = 2$, both $\langle \Omega_x^{F(0)} \rangle$ and $\langle \Omega_x^{F(T)} \rangle$ show similar curves as functions of Ω_x , even when Ω_x is small. On the other hand, for $\xi/a = 6$, $\langle \Omega_x^{F(T)} \rangle$ deviates

from $\langle \Omega_x^{F(0)} \rangle$ when Ω_x is small. The contrast between the two fitting schemes is more evident in Fig. 11(b). For the clean QPC model, $l_{\text{QPC}}^{F(T)} = l_{\text{QPC}}$ and the deviation from $l_{\text{QPC}}^{F(0)}$ is clearer when l_{QPC} is increased. On the other hand, for $\xi/a = 2$, both $l_{\text{QPC}}^{F(T)}$ and $l_{\text{QPC}}^{F(0)}$ show similar trends, even when l_{QPC} is increased. This is distinct from the clean QPC limit. For $\xi/a = 6$, intermediate results are obtained. When l_{QPC} is small, $\langle l_{\text{QPC}}^{F(0/T)} \rangle$ follows a similar curve for $l_{\text{QPC}}^{F(0/T)}$ of the clean QPC limit. When l_{QPC} is increased, $\langle l_{\text{QPC}}^{F(T)} \rangle$ deviates clearly from $l_{\text{QPC}}^{F(T)}$ of the clean QPC limit, while $\langle l_{\text{QPC}}^{F(0)} \rangle$ stays close to $l_{\text{QPC}}^{F(0)}$ of the clean QPC limit. The experiment in Ref. [27] claims that both fittings follow a similar trend, which indicates that the disorder potential scattering is very effective, as in the results of $\xi/a = 2$. Otherwise, the difference between the two fittings can be noticed.

IX. TWO-DIMENSIONAL QPC MODEL

In the experiments, QPCs are fabricated on two-dimensional (2D) electron systems. Then, the 1D tight-binding model that has been discussed might not be relevant to compare with the experimental results. In this section, we show that the main results of the fitting curvature by the 1D model are consistent with those by 2D QPC systems.

We model the QPC system with a 2D tight-binding model with the integer lattice coordinates (i, j) that has the real-space coordinates $(x, y) = (a(i - N), a(j - W/2))$, where $0 \leq i < 2N$ with $N = 100$ as in the 1D model, and $0 \leq j < W$, where W gives the width of the QPC. The QPC

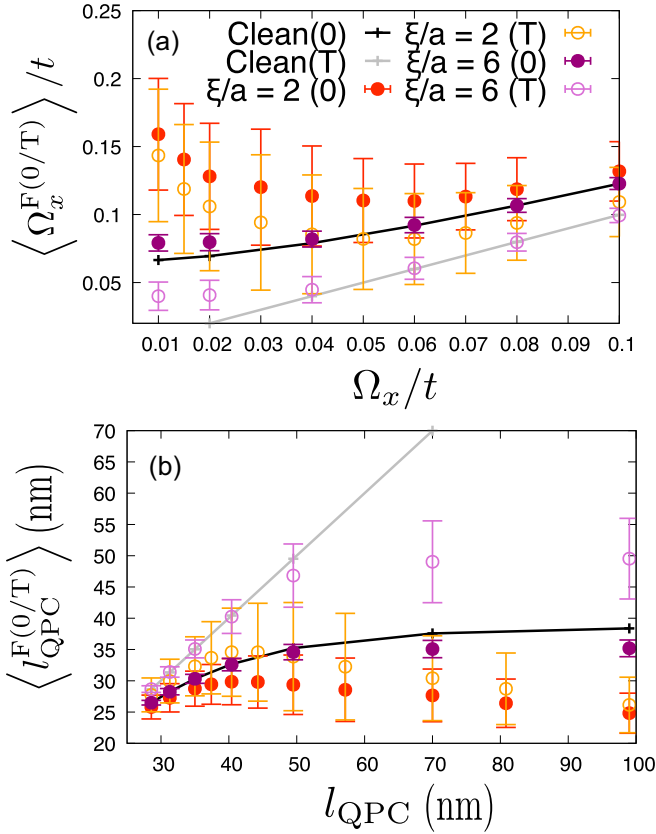


FIG. 11. Finite-temperature fitting compared to the zero-temperature fitting: (a) fitting curvature $\langle \Omega_x^{F(0/T)} \rangle$ versus Ω_x and (b) $\langle l_{\text{QPC}}^{F(0/T)} \rangle$ versus l_{QPC} . The notation of (0/T) refers to the zero- or finite-temperature fitting.

confinement potential $V_{\text{QPC}}(x, y)$ is given by

$$V_{\text{QPC}}(x, y) = V_{\text{1D}}(x) + V_{\text{2D}}(x, y), \quad (23)$$

where $V_{\text{1D}}(x)$ is the 1D QPC potential (1) near the QPC center that is smoothly terminated, as in Eq. (5), and we choose the 2D confinement potential V_{2D} as follows [35]:

$$V_{\text{2D}} = \sum_{\pm} \frac{m\omega_y^2}{2} \{y - y_{\pm}(x)\}^2 \Theta(y^2 - y_{\pm}(x)^2) \quad (24)$$

with

$$y_{\pm} = \pm \frac{Wa}{4} \left(1 - \cos \frac{\pi x}{Na}\right), \quad (25)$$

where $\Theta(x)$ is a step function: $\Theta(x) = 1$ for $x > 0$, 0 for $x < 0$. $\hbar\omega_y$ is denoted by Ω_y . We set the Fermi energy E_F the same as in the 1D model. We choose $\Omega_y/t = 0.20$, which corresponds to 2.3 meV, consistent with the experimental value [27]. The numerical calculations are performed using the KWANT code [41]. Figure 12(a) depicts $V_{\text{QPC}}(x, y)$ with $W = 80$.

The Gaussian correlated disorder potential is also extended in two dimensions with the form

$$V(x, y) = \sum_{i,j} \frac{V_{\text{md}}(i, j)}{\sqrt{\pi}\xi} \exp(-(x - x(i))^2 / 2\xi^2) \times \exp(-(y - y(j))^2 / (2\xi^2)), \quad (26)$$

where the impurities are displaced at the points $x(i)$ and $y(j)$. The random potential V_{md} is an Anderson on-site disorder potential: $\langle V_{\text{md}}(i, j)V_{\text{md}}(i', j') \rangle \equiv \Delta^2 \delta_{ii'} \delta_{jj'}$. Figure 12(b) depicts $V(x, y)$ with $\xi/a = 2$ and $\Delta/t = 0.04$.

In order to compare with the 1D model, it is necessary to define the curvature in the 2D model that corresponds to Ω_x of the 1D model. In the 2D structure, this curvature varies depending on the QPC geometry. Here, we focus on the change of the 2D QPC curvature as a result of the change in W . For this purpose, the contribution from the 1D curvature in V_{QPC} is minimized: $\Omega_x/t = 5.0 \times 10^{-3}$. In the inset of Fig. 12(c), G is plotted as a function of V_0 for the clean QPC potential at zero temperature, showing multiple conductance plateaus. To compare with the 1D model calculations, we focus on the curvature in the range $0 \leq G \leq 2e^2/h$, which corresponds to Ω_x of the 1D model, and is denoted by $\Omega_{x,2\text{D}}$. In Fig. 12, $\Omega_{x,2\text{D}}$ is plotted as a function of W . When W is increased, the potential difference between the QPC center and the leads is increased, leading to the enhancement of $\Omega_{x,2\text{D}}$.

Now we introduce the disorder potential. The numerical calculations are performed at $T = 1.4$ K as in the 1D model. The fitting function (15) is applied for the G - V_0 curve in the range $0 \leq G \leq 2e^2/h$. In Fig. 12(d), the blue points show the numerical result of G as a function of V_0 for a given disorder potential and the orange line indicates the fitting curve. For 100 disorder samples, the yield criteria (16) is applied and the statistical average is taken over the accepted samples as in the 1D model.

In Figs. 12(e) and 12(f), the main results of this section are shown: $\langle \Omega_x^F \rangle$ versus $\Omega_{x,2\text{D}}$, and $\langle l_{\text{QPC}}^F \rangle$ versus l_{QPC} that is determined by $\Omega_{x,2\text{D}}$ instead of Ω_x for the 1D model, respectively. The solid lines are the results of the clean QPC at 1.4 K. We choose the same values of ξ/a and Δ/t as in the 1D model. Those figures are compared with Figs. 4(f) and 4(g) for the 1D model. Both models yield similar results, although, in more detail, the 2D model has a smaller deviation from the clean QPC limit than the 1D model. This consistency between the results of the 1D and 2D models can be understood by Fig. 12(d). The enhancement of $\langle \Omega_x^F \rangle$ comes from the shoulder structures in G as in Fig. 10(b) of the 1D model. In summary, the 1D model does capture the essence of the 2D QPC model. Thus, the 1D model can be used to understand the 2D QPC experiment results.

X. CONCLUSIONS AND FUTURE DIRECTIONS

In this work, we investigate the QPC potential curvature under disorder potentials via the gate voltage dependence of the conductance using a noninteracting one-dimensional tight-binding model. We consider the disorder potential with Gaussian correlations characterized by the disorder strength and the spatial correlation length. The fitting potential curvature from the conductance curve is substantially deviated from the original curvature of the QPC confinement potential when the characteristic length of the QPC is larger than the disorder correlation length. The fitting curvature can even be enhanced as the QPC curvature decreases. Similar results hold in a two-dimensional QPC tight-binding model. The disorder potential produces multiple peaks on the top of the QPC. A double

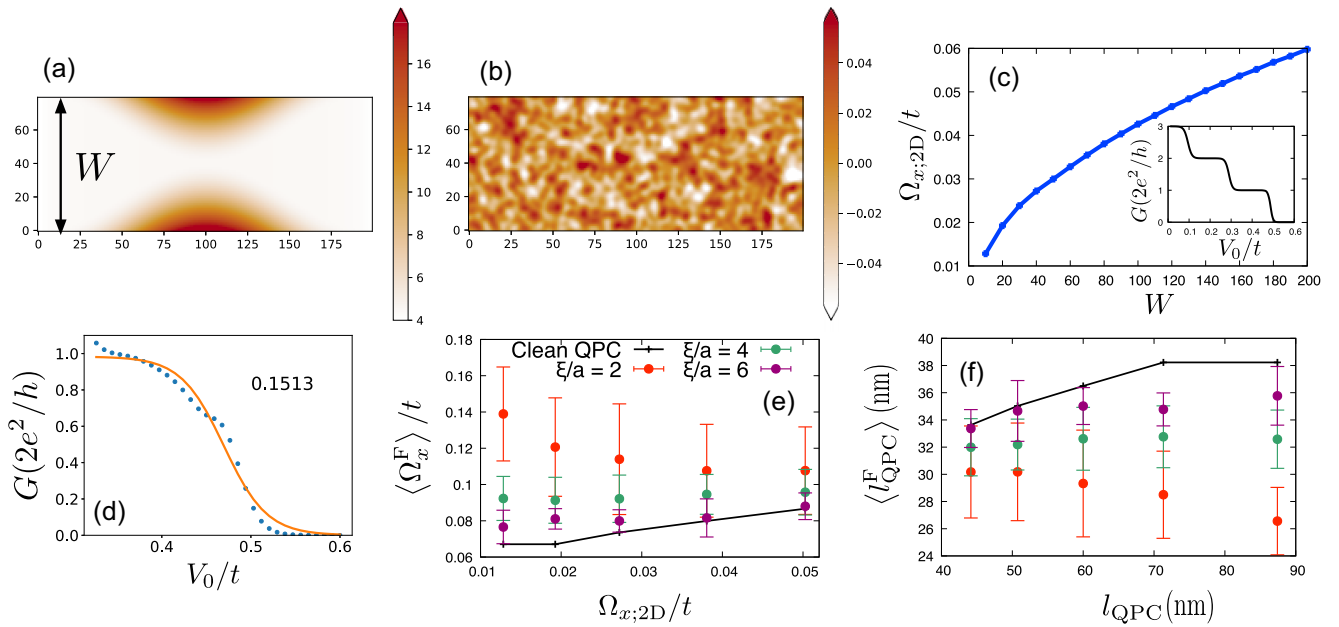


FIG. 12. QPC curvature under disorder potentials in two dimensions: (a) 2D QPC confinement potential with the QPC width $W = 80$. (b) Correlated disorder potential with $\xi/a = 2$ and $\Delta/t = 0.04$. (c) The QPC curvature $\Omega_{x;2D}$ of the G - V_0 curve in the range $0 \leq G \leq 2e^2/h$ versus W . Inset: G versus V_0 with $W = 80$ at zero temperature. (d) G versus V_0 with the disorder potential at $T = 1.4$ K with $W = 80$, $\xi/a = 2$, and $\Delta/t = 0.04$. The blue points represent the numerical result and the orange line represents the fitting curve. The value of Ω_x^F/t is indicated in the figure. (e) $\langle \Omega_x^F \rangle / t$ versus $\Omega_{x;2D}$ for various values of ξ with $\Delta/t = 0.04$. The error bars represent the variance of $\langle \Omega_x^F \rangle$. The values of $\Omega_{x;2D}$ are those for $W = 10, 20, 40, 80$, and 140 in (c). (f) $\langle l_{QPC}^F \rangle$ versus l_{QPC} that is determined by $\Omega_{x;2D}$ for the same values of ξ and Δ in (e). The solid lines represent the results for the clean QPC in (e) and (f).

barrier model is examined to demonstrate the enhancement of the fitting curvature. The results obtained are consistent with those in a recent experimental report [27]. We also discussed finite-temperature effects under the disorder potentials. The background disorder potential fluctuations are an important element of electron transport through a QPC in the transient regime between the conductance plateaus.

We should comment on the electron-electron interaction effect, which is essential in the 0.7 anomaly [42]. The details of the QPC potential can play an important role in the 0.7 anomaly. In fact, in recent experiments [5,6], the coexistence of the Fabry-Pérot oscillation and the 0.7 anomaly have been observed. In this work, we focus on the disorder effect of QPC electron transport. The interplay with the electron correlations is a very important issue, particularly for the 0.7 anomaly. In Ref. [27], the 0.7 anomaly and QPC geometry are discussed in detail, where the anomaly is dependent on the curvature. The geometrical dependence of the anomaly

has also been discussed in recent works [5,43–45]. Screening due to the Coulomb interaction modifies the effective QPC potential profile, and the effective QPC length deviates from the original QPC length. In addition, the Coulomb interaction can introduce an appropriate length scale. This extra length scale will compete with the disorder length scale discussed in this work. This interplay influences electron transport through the QPC. These issues are left for future work.

ACKNOWLEDGMENTS

T.A. acknowledges financial support from KAKENHI Grants-in-Aid (Grants No. 20K03814, No. 16H01047, and No. 15K05120). M.H.F. acknowledges financial support from a KAKENHI Grant-in-Aid (Grant No. 17H02728). Y.H. acknowledges financial support from KAKENHI Grants-in-Aid (Grants No. 18H01811, No. 15K21727, and No. 15H05867).

- [1] B. J. van Wees, H. van Houten, C. W. J. Beenakker, J. G. Williamson, L. P. Kouwenhoven, D. van der Marel, and C. T. Foxon, Quantized Conductance of Point Contacts in a Two-Dimensional Electron Gas, *Phys. Rev. Lett.* **60**, 848 (1988).
 [2] D. A. Wharam, T. J. Thornton, R. Newbury, M. Pepper, H. Ahmed, J. E. F. Frost, D. G. Hasko, D. C. Peacock, D. A. Ritchie, and G. A. C. Jones, One-dimensional transport and the quantisation of the ballistic resistance, *J. Phys. C: Solid State Phys.* **21**, L209 (1988).

- [3] M. Büttiker, Y. Imry, R. Landauer, and S. Pinhas, Generalized many-channel conductance formula with application to small rings, *Phys. Rev. B* **31**, 6207 (1985).
 [4] M. Büttiker, Quantized transmission of a saddle-point constriction, *Phys. Rev. B* **41**, 7906 (1990).
 [5] J. Heyder, F. Bauer, E. Schubert, D. Borowsky, D. Schuh, W. Wegscheider, J. von Delft, and S. Ludwig, Relation between the 0.7 anomaly and the Kondo effect: Geometric crossover

- between a quantum point contact and a Kondo quantum dot, *Phys. Rev. B* **92**, 195401 (2015).
- [6] S. Maeda, S. Miyamoto, M. H. Fauzi, K. Nagase, K. Sato, and Y. Hirayama, Fabry-Pérot interference in a triple-gated quantum point contact, *Appl. Phys. Lett.* **109**, 143509 (2016).
- [7] N. F. Ahmad, K. Komatsu, T. Iwasaki, K. Watanabe, T. Taniguchi, H. Mizuta, Y. Wakayama, A. M. Hashim, Y. Morita, S. Moriyama *et al.*, Fabry-Pérot resonances and a crossover to the quantum Hall regime in ballistic graphene quantum point contacts, *Sci. Rep.* **9**, 3031 (2019).
- [8] J. G. Williamson, C. E. Timmering, C. J. P. M. Harmans, J. J. Harris, and C. T. Foxon, Quantum point contact as a local probe of the electrostatic potential contours, *Phys. Rev. B* **42**, 7675 (1990).
- [9] A. M. See, I. Pilgrim, B. C. Scannell, R. D. Montgomery, O. Klochan, A. M. Burke, M. Aagesen, P. E. Lindelof, I. Farrer, D. A. Ritchie, R. P. Taylor, A. R. Hamilton, and A. P. Micolich, Impact of Small-Angle Scattering on Ballistic Transport in Quantum Dots, *Phys. Rev. Lett.* **108**, 196807 (2012).
- [10] M. A. Topinka, B. J. LeRoy, S. E. J. Shaw, E. J. Heller, R. M. Westervelt, K. D. Maranowski, and A. C. Gossard, Imaging coherent electron flow from a quantum point contact, *Science* **289**, 2323 (2000).
- [11] M. A. Topinka, B. J. LeRoy, R. M. Westervelt, S. E. J. Shaw, R. Fleischmann, E. J. Heller, K. D. Maranowski, and A. C. Gossard, Coherent branched flow in a two-dimensional electron gas, *Nature (London)* **410**, 183 (2001).
- [12] N. Aoki, C. R. da Cunha, R. Akis, D. K. Ferry, and Y. Ochiai, Scanning gate microscopy investigations on an InGaAs quantum point contact, *Appl. Phys. Lett.* **87**, 223501 (2005).
- [13] C. R. da Cunha, N. Aoki, T. Morimoto, Y. Ochiai, R. Akis, and D. K. Ferry, Imaging of quantum interference patterns within a quantum point contact, *Appl. Phys. Lett.* **89**, 242109 (2006).
- [14] K. E. Aidala, R. E. Parrott, T. Kramer, E. J. Heller, R. M. Westervelt, M. P. Hanson, and A. C. Gossard, Imaging magnetic focusing of coherent electron waves, *Nat. Phys.* **3**, 464 (2007).
- [15] M. P. Jura, M. A. Topinka, L. Urban, A. Yazdani, H. Shrikman, L. N. Pfeiffer, K. W. West, and D. Goldhaber-Gordon, Unexpected features of branched flow through high-mobility two-dimensional electron gases, *Nat. Phys.* **3**, 841 (2007).
- [16] S. Schnez, C. Rössler, T. Ihn, K. Ensslin, C. Reichl, and W. Wegscheider, Imaging the lateral shift of a quantum point contact using scanning gate microscopy, *Phys. Rev. B* **84**, 195322 (2011).
- [17] N. Aoki, C. R. da Cunha, R. Akis, D. K. Ferry, and Y. Ochiai, Scanning gate imaging of a disordered quantum point contact, *J. Phys.: Condens. Matter* **26**, 193202 (2014).
- [18] P. Liu, F. Martins, B. Hackens, L. Desplanque, X. Wallart, M. G. Pala, S. Huant, V. Bayot, and H. Sellier, Formation of quantum dots in the potential fluctuations of InGaAs heterostructures probed by scanning gate microscopy, *Phys. Rev. B* **91**, 075313 (2015).
- [19] B. Brun, F. Martins, S. Faniel, B. Hackens, G. Bachelier, A. Cavanna, C. Ulysse, A. Ouerghi, U. Gennser, D. Mailly, S. Huant, V. Bayot, M. Sanquer, and H. Sellier, Wigner and Kondo physics in quantum point contacts revealed by scanning gate microscopy, *Nat. Commun.* **5**, 4290 (2014).
- [20] J. A. Nixon and J. H. Davies, Potential fluctuations in heterostructure devices, *Phys. Rev. B* **41**, 7929 (1990).
- [21] M. Stopa, Quantum dot self-consistent electronic structure and the Coulomb blockade, *Phys. Rev. B* **54**, 13767 (1996).
- [22] J. A. Nixon, J. H. Davies, and H. U. Baranger, Breakdown of quantized conductance in point contacts calculated using realistic potentials, *Phys. Rev. B* **43**, 12638 (1991).
- [23] I. I. Yakimenko and K.-F. Berggren, Probing dopants in wide semiconductor quantum point contacts, *J. Phys.: Condens. Matter* **28**, 105801 (2016).
- [24] Q. Qian, J. Nakamura, S. Fallahi, G. C. Gardner, J. D. Watson, and M. J. Manfra, High-temperature resistivity measured at $\nu = \frac{5}{2}$ as a predictor of the two-dimensional electron gas quality in the $n = 1$ Landau level, *Phys. Rev. B* **95**, 241304(R) (2017).
- [25] H. Al-Taie, L. W. Smith, B. Xu, P. See, J. P. Griffiths, H. E. Beere, G. A. C. Jones, D. A. Ritchie, M. J. Kelly, and C. G. Smith, Cryogenic on-chip multiplexer for the study of quantum transport in 256 split-gate devices, *Appl. Phys. Lett.* **102**, 243102 (2013).
- [26] L. W. Smith, H. Al-Taie, F. Sfigakis, P. See, A. A. J. Lesage, B. Xu, J. P. Griffiths, H. E. Beere, G. A. C. Jones, D. A. Ritchie, M. J. Kelly, and C. G. Smith, Statistical study of conductance properties in one-dimensional quantum wires focusing on the 0.7 anomaly, *Phys. Rev. B* **90**, 045426 (2014).
- [27] L. W. Smith, H. Al-Taie, A. A. J. Lesage, K. J. Thomas, F. Sfigakis, P. See, J. P. Griffiths, I. Farrer, G. A. C. Jones, D. A. Ritchie, M. J. Kelly, and C. G. Smith, Effect of Split Gate Size on the Electrostatic Potential and 0.7 Anomaly within Quantum Wires on a Modulation-Doped GaAs/AlGaAs Heterostructure, *Phys. Rev. Appl.* **5**, 044015 (2016).
- [28] T. Ando and Y. Uemura, Theory of quantum transport in a two-dimensional electron system under magnetic fields. I. Characteristics of level broadening and transport under strong fields, *J. Phys. Soc. Jpn.* **36**, 959 (1974).
- [29] T. Ohtsuki and Y. Ono, Potential range dependence of mixing of edge states in quantum Hall effect, *J. Phys. Soc. Jpn.* **58**, 3863 (1989).
- [30] K. Richter, D. Ullmo, and R. A. Jalabert, Smooth-disorder effects in ballistic microstructures, *Phys. Rev. B* **54**, R5219 (1996).
- [31] T. Koschny and L. Schweitzer, Levitation of quantum Hall critical states in a lattice model with spatially correlated disorder, *Phys. Rev. B* **67**, 195307 (2003).
- [32] T. Kawarabayashi, Y. Ono, T. Ohtsuki, S. Kettemann, A. Struck, and B. Kramer, Unconventional conductance plateau transitions in quantum Hall wires with spatially correlated disorder, *Phys. Rev. B* **75**, 235317 (2007).
- [33] O. Goulko, F. Bauer, J. Heyder, and J. von Delft, Effect of Spin-Orbit Interactions on the 0.7 Anomaly in Quantum Point Contacts, *Phys. Rev. Lett.* **113**, 266402 (2014).
- [34] P. Stano, T. Aono, and M. Kawamura, Dipolelike dynamical nuclear spin polarization around a quantum point contact, *Phys. Rev. B* **97**, 075440 (2018).
- [35] T. Ando, Quantum point contacts in magnetic fields, *Phys. Rev. B* **44**, 8017 (1991).
- [36] L. W. Smith, H. Al-Taie, A. A. J. Lesage, F. Sfigakis, P. See, J. P. Griffiths, H. E. Beere, G. A. C. Jones, D. A. Ritchie, A. R. Hamilton, M. J. Kelly, and C. G. Smith, Dependence of the 0.7 anomaly on the curvature of the potential barrier in quantum wires, *Phys. Rev. B* **91**, 235402 (2015).

- [37] E. Jones, T. Oliphant, P. Peterson *et al.*, SciPy: Open source scientific tools for PYTHON, <http://www.scipy.org/>.
- [38] $\epsilon(j) = 0$ when $|j| \geq N$.
- [39] To perform the fitting at finite temperature, we use `scipy.integrate.quad` [37] with the integration range from $-10k_B T$ to $10k_B T$.
- [40] $\langle \Omega_x^{F(0)} \rangle = \langle \Omega_x^F \rangle$, and $I_{\text{QPC}}^{F(0)} = I_{\text{QPC}}^F$.
- [41] C. W. Groth, M. Wimmer, A. R. Akhmerov, and X. Waintal, KWANT: A software package for quantum transport, *New J. Phys.* **16**, 063065 (2014).
- [42] K. J. Thomas, J. T. Nicholls, M. Y. Simmons, M. Pepper, D. R. Mace, and D. A. Ritchie, Possible Spin Polarization in a One-Dimensional Electron Gas, *Phys. Rev. Lett.* **77**, 135 (1996).
- [43] C. Rössler, S. Baer, E. de Wiljes, P. L. Ardel, T. Ihn, K. Ensslin, C. Reichl, and W. Wegscheider, Transport properties of clean quantum point contacts, *New J. Phys.* **13**, 113006 (2011).
- [44] F. Bauer, J. Heyder, E. Schubert, D. Borowsky, D. Taubert, B. Bruognolo, D. Schuh, W. Wegscheider, J. von Delft, and S. Ludwig, Microscopic origin of the ‘0.7-anomaly’ in quantum point contacts, *Nature (London)* **501**, 73 (2013).
- [45] M. J. Iqbal, R. Levy, E. J. Koop, J. B. Dekker, J. P. de Jong, J. H. M. van der Velde, D. Reuter, A. D. Wieck, R. Aguado, Y. Meir, and C. H. van der Wal, Odd and even Kondo effects from emergent localization in quantum point contacts, *Nature (London)* **501**, 79 (2013).